Penetrating electric field with/without disturbed electric fields During the 7-8 July 2022 geomagnetic storm simulated by MAGE and observed by ICON MIGHTI

Qian Wu, Dong Lin, Wenbin Wang, Kevin Pham, Liying Qian, Haonan Wu
HAO/NCAR
3090 Center Green Dr.
Boulder, CO 80301, USA

Thomas J. Immel
Space Sciences Laboratory
U. C. Berkeley
Berkeley, CA 94720-7450, USA

Erdal Yigit
Department of Physics and Astronomy
George Mason University
Fairfax, Virginia, 22030, USA

Key Points

- The July 2022 geomagnetic storm with both externally and internally imposed electric potentials is investigated.
- Both MAGE and ICON show the development of regionally strong westward zonal winds and co-incident upward ion drift.
- MAGE simulated zonal wind changes are delayed compared with the ICON observations.

Abstract

Penetrating and disturbed electric fields develop during geomagnetic storms and are effective in driving remarkable changes in the nightside low latitude ionosphere over varying time periods. While the former arrive nearly instantaneously with the changes in the solar wind electric field, the latter take more time, requiring auroral heating to modify upper atmospheric winds globally, leading to changes in the thermospheric wind dynamo away from the auroral zones. Such changes always differ from the quiet time state where the winds are usually patterned after daytime solar heating. We use the Multiscale Atmosphere-Geospace Environment model (MAGE) and observations from the NASA Ionospheric Connection Explorer (ICON) mission to investigate both during the 7-8 July 2022 geomagnetic storm event. The model was able to simulate the penetrating and disturbed electric fields. The simulations showed enhanced westward winds and the wind dynamo induced upward ion drift confirmed by the ICON zonal wind and ion drift observations. The simulated zonal wind variations are slightly later in arrival at the low latitudes. We also see the penetrating electric field opposes or cancels the disturbed electric field in the MAGE simulation.

Plain Language Abstract

Using a numerical model where the coupled physical processes of the magnetosphere, ionosphere, and thermosphere are represented, we simulated the nighttime ionospheric disturbances caused by electric fields that enter this system from the magnetosphere and electric fields generated internally by changes in the thermospheric winds. The former is quick to reach the low latitudes, and the latter is delayed by the slower response of the neutral winds. The coupled model and NASA satellite observation showed good agreement. The results show good capability and lend themselves to the future effort to forecast space weather at low latitudes.

Introduction

The penetrating electric field is induced by interplanetary magnetic field (IMF) southward turning or other IMF variation related sudden increase of the cross polar cap potential (CPCP). The subsequent storm time thermospheric winds can induce the disturbed electric field in the low latitude ionosphere [e.g., Kelley et al., 2003; Kikuchi et al., 2008]. Penetrating electric field can reach the equatorial region nearly instantaneously, whereas the effects of the disturbed electric field originating in the modified neutral wind dynamo takes hours to develop [Richmond and Matsushita, 1975; Blanc and Richmond, 1980; Richmond et al., 2003; Fejer et al, 1983; 2007; 2008]. The disturbed nighttime electric fields are driven by a westward thermospheric wind disturbance that expands from high latitudes, leading to an eastward electric field and an upward ion drift.

Wu et al [2022; 2024a] have shown that the MAGE model is capable of simulating the penetrating electric field because of its more dynamic high latitude input from the GAMERA (Grid Agnostic MHD with Extended Research Applications) magnetosphere model compared to traditional empirical ion convection models such as Weimer [2005] or Heelis et al. [1982]. We have not used the MAGE model to simulate the disturbed electric field before. Through geomagnetic storms, we may have both penetrating electric field and disturbed electric field in the low latitudes. The penetrating electric field can be superimposed on the disturbed electric field. If MAGE can simulate both electric fields, then the simulation can help resolve two interesting questions: 1) How to distinguish these two kinds of disturbances? 2) Will the penetrating electric field affect the disturbed electric field at different local times? Answers to these questions can lead to better understanding of the nightside ionosphere during storm time.

The 7-8 July 2022, geomagnetic storm offers a good opportunity to examine the interaction of the penetrating electric field with the disturbance electric field. Figure 1 shows the IMF and solar wind parameters for 7 July 2022. A sharp southward turning of the IMF Bz accompanied by a large IMF By component at about 12 UT caused the sudden onset of a strong geomagnetic storm sustained by a prolonged negative IMF Bz for the latter half of the day. The southward turning presents a chance for investigating the prompt effect of the penetrating electric field. Figure 2 shows the IMF and solar wind parameters for 8 July 2022. After a long duration of negative IMF Bz started in July 7, the IMF Bz turned northward for roughly 6 hours. While the positive IMF Bz tempered the geomagnetic storm somewhat, the geomagnetic condition was still active (Kp ~ 4). It was followed by another southward turning of IMF Bz and IMF By turning strongly negative at 7 UT presenting another opportunity to examine the prompt penetrating electric field associated with this combination of the IMF Bz negative turn and IMF By negative turn during geomagnetic active time with disturbed electric field.

To answer these aforementioned two questions, we will use the MAGE model to investigate the penetrating electric field on 7 July (~ 12 UT) and on 8 July (~ 7 UT) under different geomagnetic conditions. The first one started from a quiet time, whereas the second one occurred during more active time and disturbed electric field. The ICON MIGHTI neutral wind data will be used to investigate the source of wind dynamo in the equatorial region along with the ICON IVM in-situ vertical ion drift. The data can provide a validation of the simulation results. This is particularly important because many of the past studies lacked wind observations [e.g., Fejer et al., 2008, Richmond et al., 2003].

MAGE (Multiscale Atmosphere-Geospace Environment) Model

The MAGE model combines the magnetosphere model GAMERA (Grid Agnostic MHD with Extended Research Applications), the ring current model RCM (Rice Convection Model), and the TIEGCM (Thermospheric Ionosphere Electrodynamics General Circulation Model) [Zhang et al. 2019; Toffoletto et al. 2003; Richmond et al., 1992]. The REMIX (RE-developed Magnetosphere-Ionosphere Coupler/Solver) links the different modules together to obtain the high latitude potential and derive the electron precipitation [Merkin and Lyon, 2010]. Unlike the traditional TIEGCM driven by empirical high latitude ion convection models [Heelis et al. 1982; Weimer 2005], MAGE is more dynamic for simulating fast changing variations. Moreover, GAMERA usually demonstrates more mesoscale to small-scale structures in the polar cap like enhanced electron densities and TADs/TIDs than the empirical model. [Lin et al., 2021; Pham et al., 2022; Wang et al., 2008]. Adding the RCM helps to simulate the ring current effect. It is the source of shielding or afternoon polarization. The TIEGCM has a higher horizontal spatial resolution of 1.25 degree and vertical resolution of 0.25 scale height. The time step is 5 seconds and results are saved every 5 minutes. TIEGCM has the electrodynamics and two-way interaction between the ion and neutrals, which is more accurate depiction of the thermosphere and ionosphere dynamics.

ICON Observations

We also used thermospheric wind and ion drift data from NASA's ICON mission to compare with the MAGE simulation results [Immel et al., 2018]. ICON is an equatorial mission for studying equatorial ionospheric connection to the lower atmosphere. The MIGHTI (Michelson Interferometer for Global High-Resolution Thermospheric Imaging) instrument measures neutral winds and temperatures from mesosphere to thermosphere [Englert et al., 2017; 2023; Harding et al., 2017; 2021; Harlander et al., 2017]. In this study, the redline winds are used to examine the thermospheric winds at 250 km. The winds are measured by recording the Doppler shift in the O 630 nm redline airglow emission. The MIGHTI instrument covered both day and night times. MIGHTI has two identical instruments (A and B) pointing 45-degree forward and 45-degree backward on the right-side of the satellite track. MIGHTI combines these two orthogonal viewing measurements to form vector winds at limb-scan tangent point. The wind error is about 10 m/s [Englert et al., 2017; 2023].

The ICON IVM (Ion Velocity Meter) measures the ion drift at the satellite orbital height ~ 600 km [Heelis et al., 2017]. The instrument has two sensors RPA (Retarding Potential Analyzer) and an Ion Drift Meter (IDM). The IDM instrument determines the orientation of the incoming ion flow, whereas the RPA measures the ram direction ion flow speed. The combination of measurements from the two devices gives the ion drift vector. The ion drift error is about 4.5 m/s [Heelis et al., 2017]. The instrument outputs ExB meridional and zonal ion drift. The ExB meridional drift is in the vertical direction at the magnetic equator. It is a good approximation of the vertical ion drift in the low latitude region. We use that component to represent the vertical ion drift.

Simulations and Observations

7 July 2022 Case of Penetrating Electric Field without Disturbance Electric Field

Figure 3 shows the MAGE simulation of the high northern latitude (> 50º N) polar cap potential map from 12 to 13 UT. Because of the large positive IMF By, the duskside cell is more dominant [Weimer, 2005]. As the IMF Bz turns southward the CPCP increases from 50 kV to 109 kV. To examine the equatorial dawn-dusk potential, we extend the potential map to the equator in Figure 4. The dayside eastward electric field is enhanced due to the CPCP increase and same for the nightside westward electric field. Consequently, an enhancement is seen in the nightside downward ion drift (Figure 5). From 12 UT to 13 UT the downward ion drift nearly doubled. This case of the penetrating electric field is not as dramatic as the one in the work by Wu et al. [2022; 2024]. On the nightside the vertical ion drifts are consistently downward.

Figure 6 plots the zonal wind observed by the ICON MIGHTI and simulated by MAGE along the MIGHTI observational track during different orbits on 7 July. Additionally, the ExB meridional ion drift from ICON IVM and MAGE simulation along the orbital track are also shown on the right side. The neutral winds before 12 UT are for a quiet time with relatively small diurnal variations in the zonal winds. After 12 UT when the IMF Bz turned southward, the wind changed gradually with more noticeable enhanced westward zonal winds on the nightside. The MAGE simulated winds agree with the MIGHTI winds very well. After 12 UT, we see strong nightside westward winds (~ 300 m/s near the end of the day). We did not see noticeable disturbances in the ion drift either in the IVM data or MAGE simulation. The sampling tracks of the ICON MIGHTI and IVM are shown in Figure 7.

8 July 2022 Case of Penetrating Electric Field with Disturbed Electric Field

Figure 8 shows the polar cap potential map for 8 July 2022 between 7 UT to 8 UT. The CPCP increased from 35.5 kV to 93.5 kV from 0721 to 0831 UT. In this case, the IMF Bz was positive then dropped slightly negative (Figure 2 near the beginning of the highlighted area). Because the IMF By changed from positive to strongly negative (- 20 nT), this is also a strong negative IMF By driven case leading to the rapid increase of the CPCP. Whether is driven by IMF Bz or IMF By, the net effect is a rapid increase of the CPCP, which lead to penetrating electric field. To examine the penetrating electric field, we extend the potential map to the equator shown in Figure 9. Unlike Figure 4, the nightside potential is more complex with a potential bulge, whereas on the dayside, it is mostly an eastward electric field. On the nightside, the pre-existing bulge divides the nightside into a strong westward electric field towards dusk, and a region of eastward electric field just after midnight. Figure 10 shows the nightside equatorial vertical ion drift from 7-8 UT. We see a region of the upward ion drift corresponding to the eastward electric field. After 0730 UT, the upward ion drift diminished significantly and the downward ion drift near dawn enhanced as the result of the penetrating electric field from the elevated CPCP suppressing the upward ion drift. Now the question is whether the potential bulge is a result of the disturbed electric field from the neutral wind dynamo. Figure 11 shows the zonal wind observed by ICON MIGHTI and simulated by the MAGE. Unlike the comparison presented in Figure 6, the observed neutral wind has strong westward winds on the nightside very close to where the potential bulge is shown in Figure 9. The proximity of the strong westward winds and potential bulge adds more creditability to the notion that the bulge is linked to the wind produced disturbed electric field on the nightside. MAGE simulation agrees with the MIGHTI observation. At the beginning the MAGE simulated westward zonal wind matched the ICON observed westward wind in timing as well (the orbit started at 0.25 UT), but at later times, the timing and size discrepancies grew. Along with the zonal winds, the ExB meridional ion drifts are also plotted in the same format as in Figure 6. In this case, the MAGE ion drift disturbances are significant and occurred in proximity of the enhanced westward zonal winds between -180 and 0 deg longitudes before 10 UT. We see similar delay in the simulated ion drift disturbances compared to the ICON IVM observations.

For a more detailed comparison of zonal wind variations vs vertical ion drift (ExB meridional), we plotted one orbit from 7-8 July each with very large zonal wind variations (Figure 12). The 7 July data during quieter condition lacks large zonal wind variations in both ICON MIGHTI observations and MAGE simulations. The MAGE simulated ion drift show no large variations (black line). On the other hand, the ICON IVM instrument showed some fast variations possibly from nighttime bubbles or sources other than neutral wind dynamo (blue dots).

The 8 July data have very large westward zonal winds in both MIGHTI data and MAGE simulations, which are highlighted by light-green color. The corresponding IVM ExB meridional drift showed nearly constant ~ 50 m/s. The MAGE simulated negative zonal wind (pink line) are smaller than that from the MIGHTI. The corresponding simulated ion drift is in general smaller than that from the IVM measurements. The simulated westward zonal wind peaked later than that from the MIGHTI observations. We should note that difference between the MAGE simulations and ICON observations are all larger than the measurements errors the ICON instruments.

Discussion

The 7-8 July 2022 geomagnetic storm event provided a good opportunity to examine the penetrating electric field and disturbance electric field concurrently. Using the MAGE model, we showed the penetrating electric field affecting the equatorial region on two occasions under different geomagnetic conditions.

7 July 2022 case (Penetrating electric field without disturbed electric field)

In this quiet condition case, the IMF Bz turned southward at 12 UT, the penetrating electric field enhanced eastward (westward) electric field on the dayside (nightside). The nighttime westward electric field caused stronger downward ion drift. The vertical ion drifts are relatively uniform. The low latitude neutral winds were only gradually disturbed a few hours after the southward turning of the IMF Bz near the end of the day.

8 July 2022 case (Penetrating electric field with disturbed electric field)

During the second southward turning of the IMF Bz (the IMF By turned negative) at 7 UT on July 8, 2022, the penetrating electric field was superimposed on the existing disturbed electric field, which induced a regional upward ion drift. The penetrating electric field reduced the disturbed electric field. The neutral wind and ion drift observations from ICON and simulation from MAGE are consistent with the expected wind dynamo source for the disturbance electric field. Because of the unique combination of the ICON observations, we see that the westward zonal wind induced upward ion drift consistent with the potential bulge in the potential map. We were unable to find the ICON ion drift signature of the penetrating electric field because of the small magnitude of the field and unfavorable location of the ICON satellite. The penetrating electric field simulated by MAGE was also small as well.

The significance of the MAGE simulation is that we have shown the model can help distinguish the complex equatorial electric fields during geomagnetic storms. Overall, the MAGE simulated thermospheric neutral winds showed a very good agreement with the general morphology of ICON MIGHTI observations. It also showed the importance of the neutral wind observations, for validating global models. Without the MIGHTI observations we would not be able to confirm the existence of disturbed neutral wind dynamo simulated by the MAGE.

We see the westward zonal wind producing upward ion drift in both the ICON observations and MAGE simulations (Figure 12). We also notice that the MAGE simulated westward zonal wind disturbances are delayed and smaller compared to the ICON MIGHTI observations. It may indicate the Joule heating source the MAGE model may not be sufficiently large to drive a fast and meridional propagation with stronger zonal wind disturbance. Joule heating is a major source of energy input in the thermosphere-ionosphere system and depends highly on the latitude resolution at high-latitudes [Yiğit and Ridley, 2011]. The westward zonal wind dynamo is a cross product with equatorial magnetic field, which is mostly northward, resulting in upward ion drift. The results show that having more accurate Joule heating in the model is critically important for simulating the equatorial wind dynamo.

Westward zonal wind disturbance and link to the equatorial potential bulge

While the link between the westward zonal wind and upward ion drift (potential bulge) has been suggested by Richmond et al. [2023], we are able to confirm that with new MAGE model and observe such link in the ICON neutral wind and ion drift observations. The zonal wind does not to link to the solar wind condition directly. The substorm enhanced Joule heating pushes strong equatorward winds. Consequently, the Coriolis force pushes the zonal wind westward. The ICON observations show the MAGE simulated westward zonal wind enhancement arrived later indicating the MAGE model may not have sufficiently strong Joule heat to generate large enough equatorward winds, which would arrive low latitudes earlier. That points to the way to further improvement of the model. We also should note that we only analyzed two events, which can leave uncertainties. More analysis of these type of events with combination of observations and simulations are needed. It is unfortunate that we do not have ICON with us anymore. Hopefully, future NASA or other missions will refill the observational gap. More ground-based wind observations certainly will help to move study forward.

Summary

The 7-8 July 2022 geomagnetic storm event provides an opportunity to examine the penetrating and disturbed electric fields. We used the MAGE simulation and ICON wind and ion drift observation to investigate this event and were able to see in the simulation that the penetrating electric field suppresses the disturbed electric field on the nightside. The simulation shows that the strong westward zonal winds coincide with the upward ion drift consistent with the theory of the disturbed electric field driven by neutral wind dynamo and confirmed by ICON MIGHTI and IVM wind and ion drift observations in daytime (Immel et al., 2022, Harding et al., 2024) and in nighttime. The MAGE simulated westward winds are weaker and delayed compared to the ICON observation

Open Research

The ICON MIGHTI and IVM data can be found at the ICON Mission website https://icon.ssl.berkeley.edu/Data and in the NASA SPDF Archive (spdf.gsfc.nasa.gov/data) The MAGE simulation results along the ICON sampling tracks can be found at dataset by Wu et al. [2024b].

Acknowledgment

Q. Wu is supported by 80NSSC20K0199, 80NAAC21K0014, NNX17AG69G, 80NSSC22K0170, 80NSSC22K0016 and NSF grants AGS-2120511 and AGS-2054356. W. Wang is supported by 80NSSC20K0601, 80NSSC17K0013, 80NSSC20K0356, 80NSSC19K0080, 80NSSC17K0679, and 80NSSC20K0199. D. L. was supported by NASA DRIVE Science Center for Geospace Storms (CGS) under Grant 80NSSC22M0163, and Grants 80NSSC21K0008, 80NSSC21K1677, 80NSSC22K1635, and 80NSSC23K1055, and NASA Contract 80GSFC18C0061 to the University of Colorado, Boulder. L. Qian is supported by NASA grant 80NSSC20K0189.

References

Blanc, M., and A. Richmond (1980), The ionospheric disturbance dynamo, *J. Geophys. Res.*, 85(A4), 1669–1686, doi:10.1029/JA085iA04p01669.

Emmert, J. T., D. P. Drob, G. G. Shepherd, G. Hernandez, M. J. Jarvis, J. W. Meriwether, R. J. Niciejewski, D. P. Sipler, and C. A. Tepley (2008), DWM07 global empirical model of upper thermospheric storm-induced disturbance winds, *J. Geophys. Res.*, 113, A11319, doi:10.1029/2008JA013541.

Englert, C. R., Harlander, J. M., Brown, C. M., Marr, K. D., Miller, I. J., Stump, J. E., et al. (2017). Michelson interferometer for global high-resolution thermospheric imaging (MIGHTI): Instrument design and calibration. *Space Science Reviews*, 212(1–2), 553–584. https://doi.org/10.1007/s11214-017-0358-4

Englert, C.R., Harlander, J.M., Marr, K.D., Harding, B.J., Makela, J.J., Fae, T., Brown, C.M., Ratnam, M.V., Rao, S.V.B. and Immel, T.J., (2023). Michelson Interferometer for Global High-Resolution Thermospheric Imaging (MIGHTI) On-Orbit Wind Observations: Data Analysis and Instrument Performance. *Space Science Reviews, 219(3)*, p.27. DOI: 10.1007/s11214-023-00971-1

Fejer, B.G., Larsen, M.F. and Farley, D.T. (1983), Equatorial disturbance dynamo electric fields. Geophys. Res. Lett., 10: 537-540. https://doi.org/10.1029/GL010i007p00537

Fejer, B. G., J. W. Jensen, T. Kikuchi, M. A. Abdu, and J. L. Chau (2007), Equatorial ionospheric electric fields during the November 2004 magnetic storm, *J. Geophys. Res., 112*, A10304, doi:10.1029/2007JA012376.

Fejer, B. G., J. W. Jensen, and S.-Y. Su (2008), Seasonal and longitudinal dependence of equatorial disturbance vertical plasma drifts, *Geophys. Res. Lett.*, 35, L20106, doi:10.1029/2008GL035584.

Harding, B. J., Makela, J. J., Englert, C. R., Marr, K. D., Harlander, J. M., England, S. L., & Immel, T. J. (2017). The MIGHTI wind retrieval algorithm: Description and verification. *Space Science Reviews*, 212(1–2), 585–600. https://doi.org/10.1007/s11214-017-0359-3

Harding, B. J., Chau, J. L., He, M., Englert, C. R., Harlander, J. M., Marr, K. D., et al. (2021). Validation of ICON-MIGHTI thermospheric wind observations: 2. Green-line comparisons to specular meteor radars. *Journal of Geophysical Research: Space Physics*, 126, e2020JA028947. https://doi.org/10.1029/2020JA028947

Harlander, J. M., Englert, C. R., Brown, C. M., Marr, K. D., Miller, I. J., Zastera, V., et al. (2017). Michelson interferometer for global high-resolution thermospheric imaging (MIGHTI): Monolithic interferometer design and test. *Space Science Reviews*, 212(1–2), 601–613. https://doi.org/10.1007/s11214-017-0374-4

Heelis, R. A., J. K. Lowell, and R. W. Spiro (1982), A model of the high-latitude ionospheric convection pattern, *J. Geophys. Res.*, 87(A8), 6339–6345, doi:10.1029/JA087iA08p06339.

Heelis, R.A., Stoneback, R.A., Perdue, M.D. *et al.* Ion Velocity Measurements for the Ionospheric Connections Explorer, *Space Sci Rev* 212, 615–629 (2017). https://doi.org/10.1007/s11214-017-0383-3.

Immel, T. J., England, S. L., Mende, S. B., Heelis, R. A., Englert, C. R., Edelstein, J., et al. (2017). The ionospheric connection explorer mission: Mission goals and design. *Space Science Reviews*, 214(13). https://doi.org/10.1007/s11214-017-0449-2

Kelley, M. C., J. J. Makela, J. L. Chau, and M. J. Nicolls (2003), Penetration of the solar wind electric field into the magnetosphere/ionosphere system, *Geophys. Res. Lett., 30*(4), 1158, doi:10.1029/2002GL016321.

Kikuchi, T., K. K. Hashimoto, and K. Nozaki (2008), Penetration of magnetospheric electric fields to the equator during a geomagnetic storm, *J. Geophys. Res.*, 113, A06214, doi:10.1029/2007JA012628.

Lin, D., Sorathia, K., Wang, W., Merkin, V., Bao, S., Pham, K., et al. (2021). The role of diffuse electron precipitation in the formation of subauroral polarization streams. *Journal of Geophysical Research: Space Physics*, 126, e2021JA029792. https://doi.org/10.1029/2021JA029792

Merkin, V., & Lyon, J. (2010). Effects of the low-latitude ionospheric boundary condition on the global magnetosphere. Journal of Geophysical Research: Space Physics, 115(A10). doi: 10.1029/2010JA015461.

Pham, K. H., Zhang, B., Sorathia, K., Dang, T., Wang, W., Merkin, V., et al. (2022). Thermospheric density perturbations produced by traveling atmospheric disturbances during August 2005 storm.

Journal of Geophysical Research: Space Physics, 127, e2021JA030071. https://doi.org/10.1029/2021JA030071

Richmond, A. D., and S. Matsushita (1975), Thermospheric response to a magnetic substorm, *J. Geophys. Res.*, 80(19), 2839–2850, doi:10.1029/JA080i019p02839.

Richmond, A., Ridley, E., & Roble, R. (1992). A thermosphere/ionosphere general circulation model with coupled electrodynamics. Geophysical Research Letters, 19(6), 601–604. doi: 10.1029/92GL00401.

Richmond, A. D., C. Peymirat, and R. G. Roble (2003), Long-lasting disturbances in the equatorial ionospheric electric field simulated with a coupled magnetosphere-ionosphere-thermosphere model, *J. Geophys. Res.*, 108, 1118, doi:10.1029/2002JA009758, A3.

Toffoletto, F., Sazykin, S., Spiro, R., & Wolf, R. (2003). Inner magnetospheric modeling with the rice convection model. Space Science Reviews, 107(1-2), 175– 196. doi: 10.1023/A:1025532008047.

Wang, W., J. Lei, A. G. Burns, M. Wiltberger, A. D. Richmond, S. C. Solomon, T. L. Killeen, E. R. Talaat, and D. N. Anderson (2008), Ionospheric electric field variations during a geomagnetic storm simulated by a coupled magnetosphere ionosphere thermosphere (CMIT) model, *Geophys. Res. Lett.*, *35*, L18105, doi:10.1029/2008GL035155.

Weimer, D. R. (2005), Improved ionospheric electrodynamic models and application to calculating Joule heating rates, *J. Geophys. Res.*, 110, A05306, doi:10.1029/2004JA010884.

Wu, Q., Wang, W., Lin, D., Huang, C., & Zhang, Y. (2022), Penetrating electric field simulated by the MAGE and comparison with ICON observation. *Journal of Geophysical Research: Space Physics*, 127, e2022JA030467. https://doi.org/10.1029/2022JA030467

Wu, Q.; Wang, W.; Lin, D.; Huang, C.; Zhang, Y. (2024a), Penetrating Electric Field during the Nov 3–4, 2021 Geomagnetic Storm. J. Atmos. Sol.-Terr. Phys., 257, https://doi.org/10.1016/j.jastp.2024.106219

Wu, Qian, Dong Lin, Wenbin Wang. (2024b). Penetrating electric field with/without disturbed electric fields During the Nov 7-8, 2022 geomagnetic storm simulated by MAGE and observed by ICON MIGHTI data set. Version 1.0. UCAR/NCAR - GDEX. https://doi.org/10.5065/61wa-2010. Accessed 19 Jan 2024.

Yiğit, E., and A. J. Ridley (2011), Effects of high-latitude thermosphere heating at various scale sizes simulated by a nonhydrostatic global thermosphere ionosphere model, *J. Atmos. Sol-Terr. Phys.*, *73*, 592-600, doi:10.1016/j.jastp.2010.12.003.

Zhang, B., Sorathia, K. A., Lyon, J. G., Merkin, V. G., Garretson, J. S., & Wiltberger, M. (2019). GAMERA: A three-dimensional finite-volume MHD solver for non-orthogonal curvilinear geometries. The Astrophysical Journal Supplement Series, 244(1), 20. doi: 10.3847/1538-4365/ab3a4c.

Figure captions

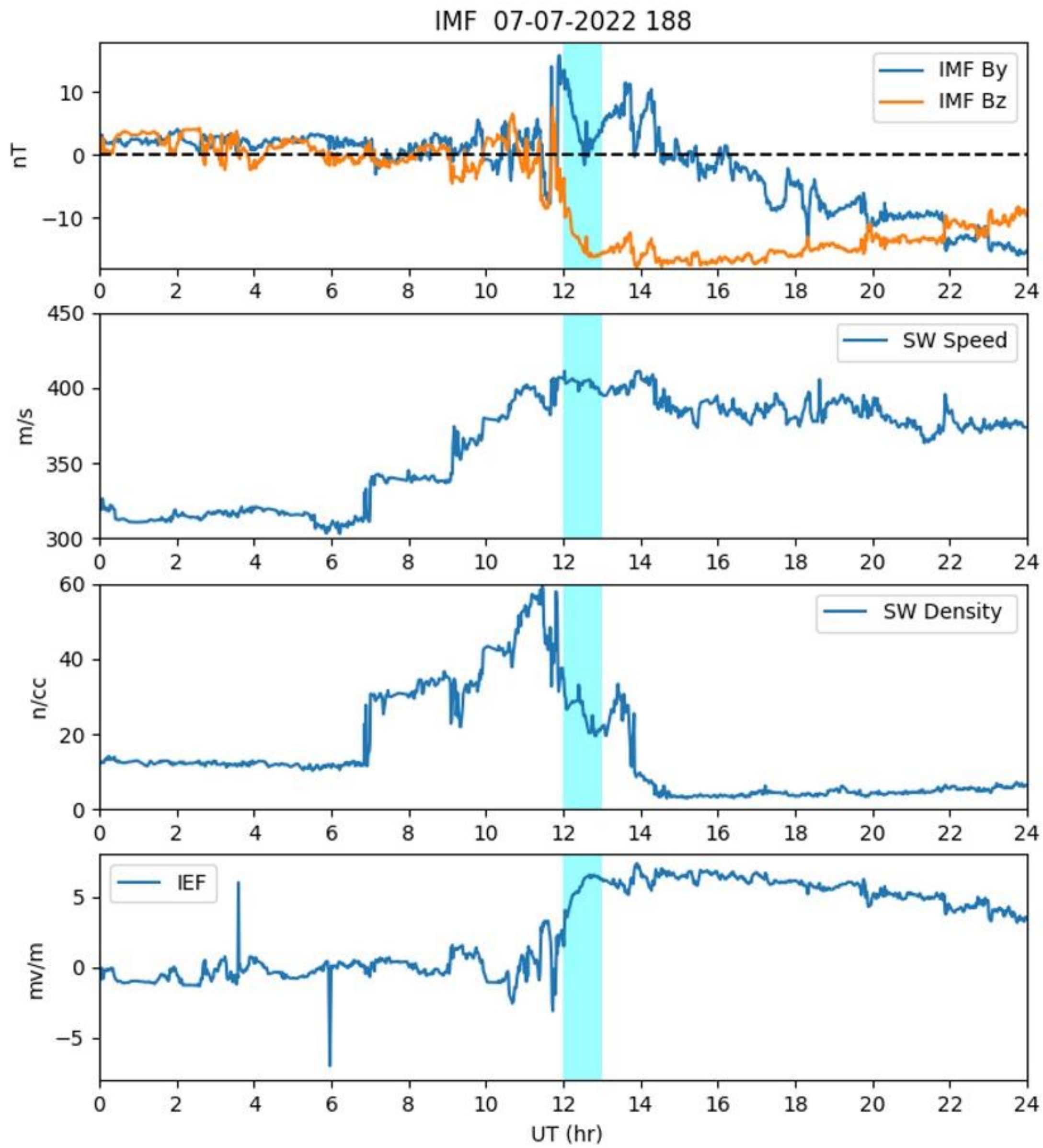

Figure 1. IMF and Solar Wind parameters for 7 July 2022. The highlighted area contains IMF Bz southward turning and positive turning of the IMF By (the first panel). While IMF changed dramatically near 12 UT, the solar wind speed (the second panel) and density (the third panel) enhancements arrived earlier. The changing of the IMF Bz led to an increase of the interplanetary electric field (IEF) in the fourth panel.

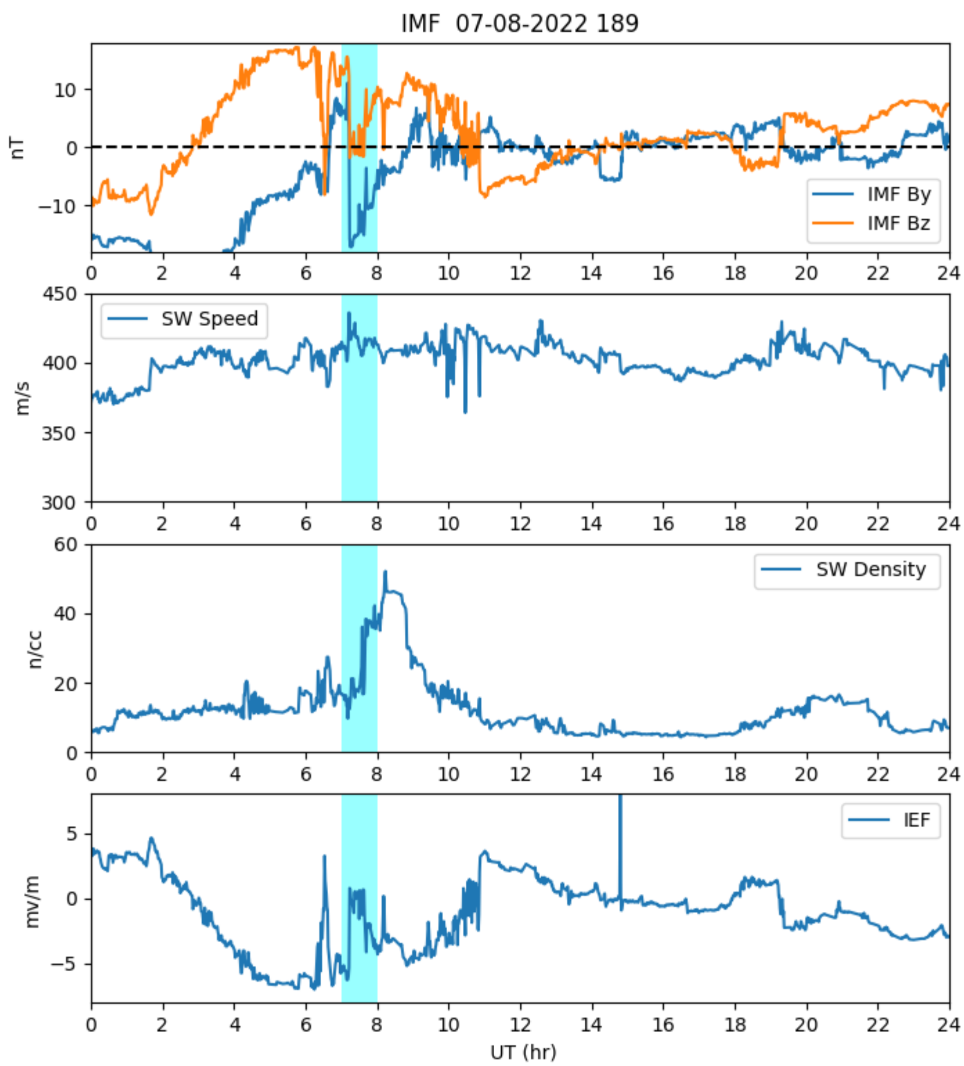

Figure 2. IMF and Solar Wind parameters for 8 July 2022

Same as Figure 1 but for July 8, 2022. The highlighted interval includes a sudden turning of the IMF Bz from large positive to near zero. The IMF By turned from positive to negative. While the solar wind speed did not change much, the density also increased. The IEF changed from negative to positive.

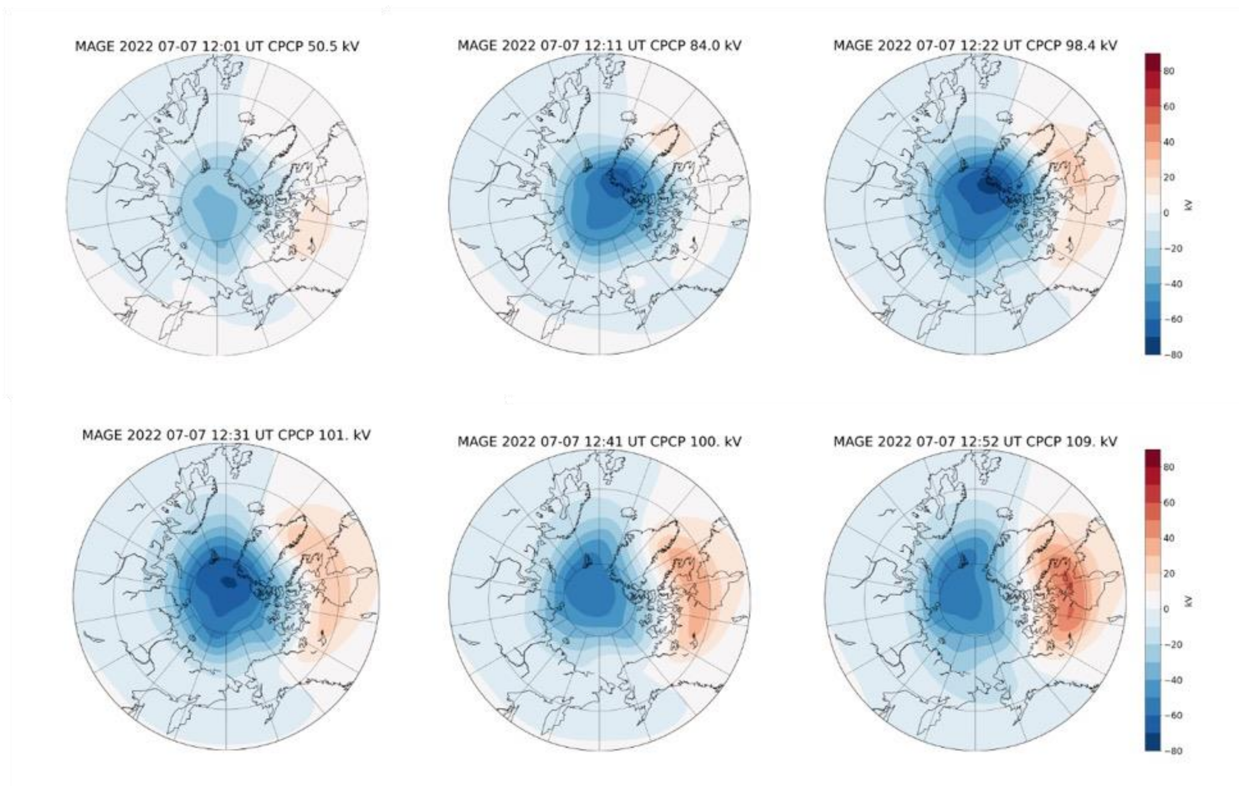

Figure 3. 7 July 2022 at 12-13 UT, potential map over northern polar region (> 50N). The cross polar cap potential increased from 50 kV to 84 kV from 1201 UT to 1211 UT in response to the southward turning of the IMF Bz at 1200 UT. Because of the large IMF By component there is a very large duskside convection cell, which became more symmetric with the dawnside cell near 12:52 UT as the IMF By dropped to close to zero.

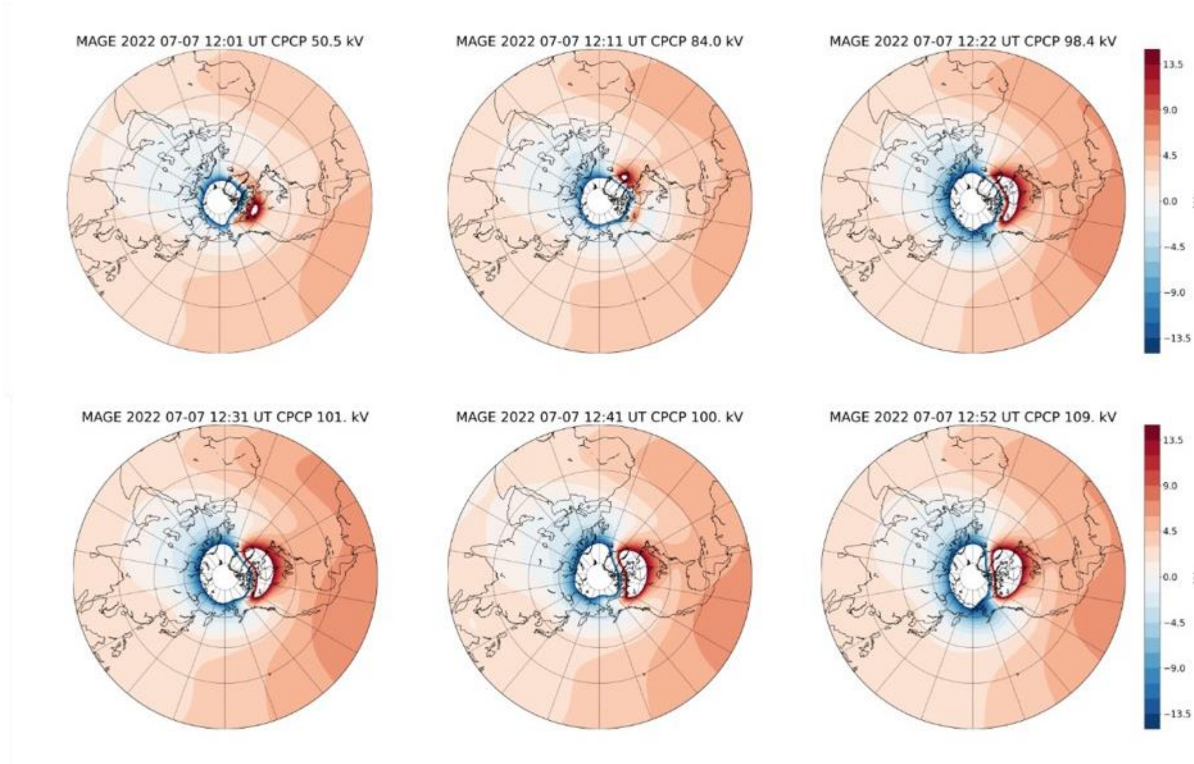

Figure 4. 7 July 2022 at 12-13 UT, potential map for the northern hemisphere. By extending the potential map to the equator, we can see the dawn-dusk potential by counting the contour steps. Even though the CPCP reached 85 kV, the dawn-dusk potential difference only increased when the dawnside cell started to form. Overall increase of the dawn-dusk potential drop (1.5 kV one contour step) is not large. The small increase is a result of the penetrating electric field.

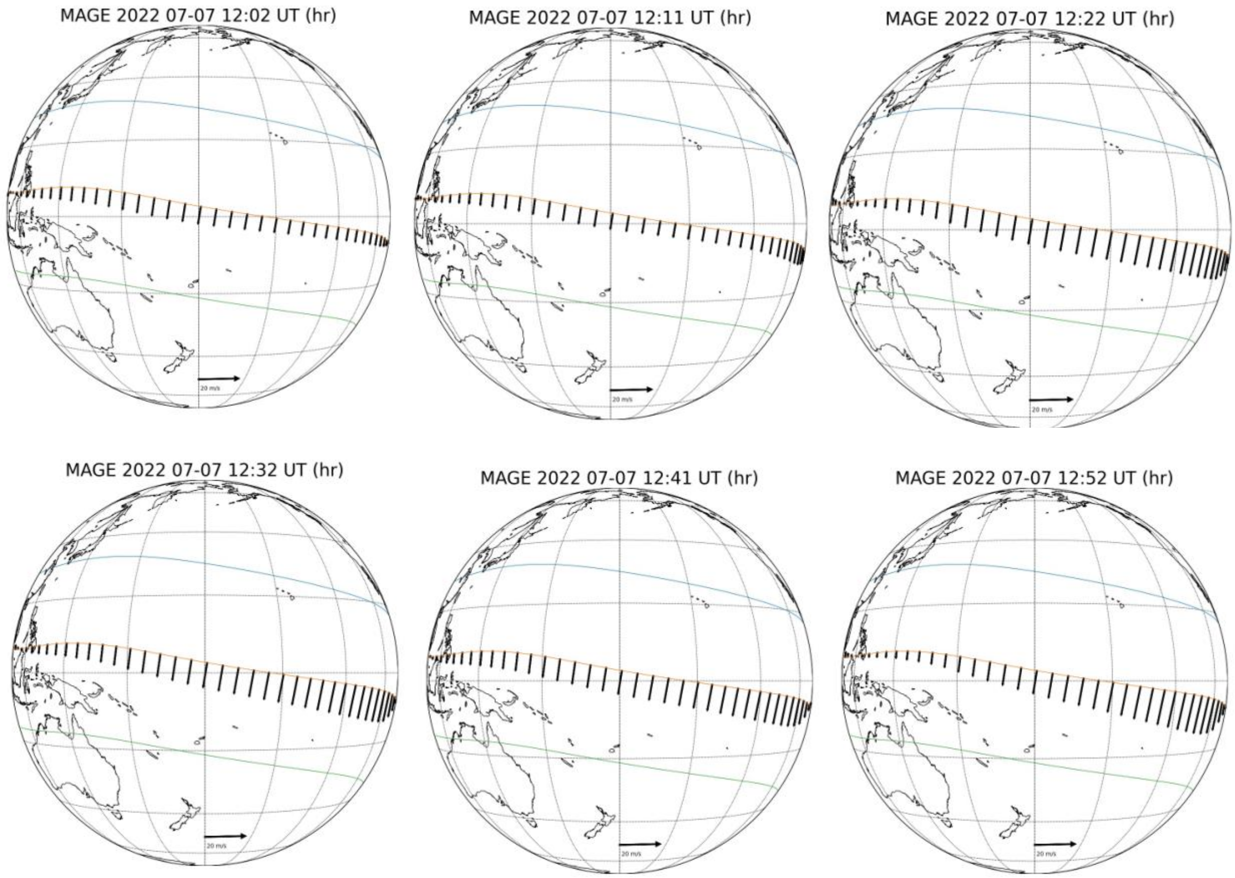

Figure 5. 7 July at 12-13 UT nightside equatorial vertical ion drift. The nightside downward drift is consistent with the westward electric field. The enhancement of downward drift reflects the increase of the dawn-dusk potential drop from penetrating electric field Mid-night is in the middle of plot.

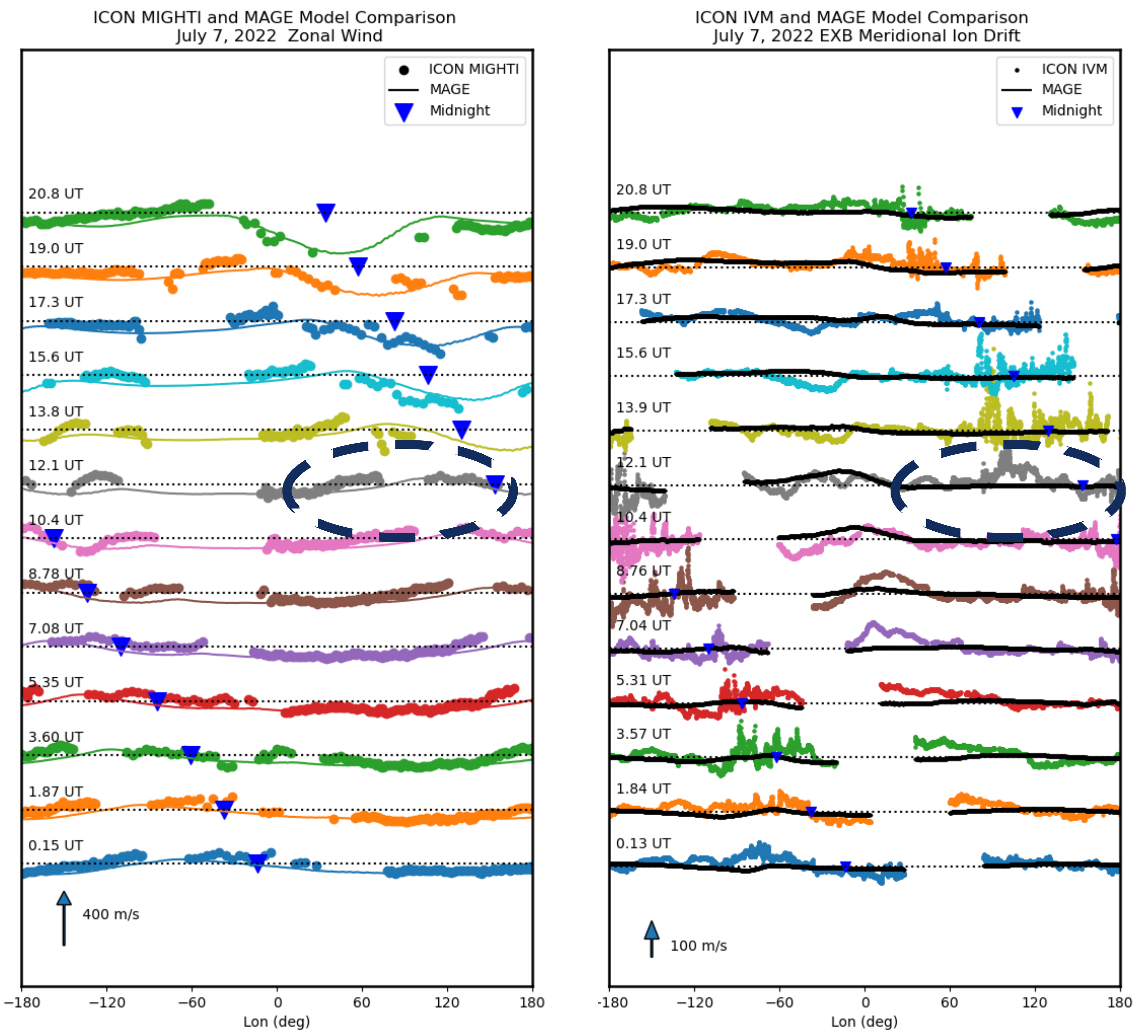

Figure 6. 7 July, MAGE simulation and ICON observation of zonal thermospheric winds and ion drifts. ICON MIGHTI observed zonal wind and MAGE simulations along the MIGHTI sampling points (right) are plotted. Data from each orbit are plotted according to the longitude. The starting time for each orbit is provided. The midnight is marked by blue triangles. MIGHTI data gaps are due to SAA (South Atlantic Anomaly) or day-night transitions (see Englert et al., 2023). The IMF Bz southward turning occurred after 12 UT, which is highlighted by a dashed oval. The nightside

zonal wind start to see reaction in the next orbit. Not much change is seen on the dayside. The ExB meridional ion drifts (vertical upward at the magnetic equator) for each orbit are plotted on the right.

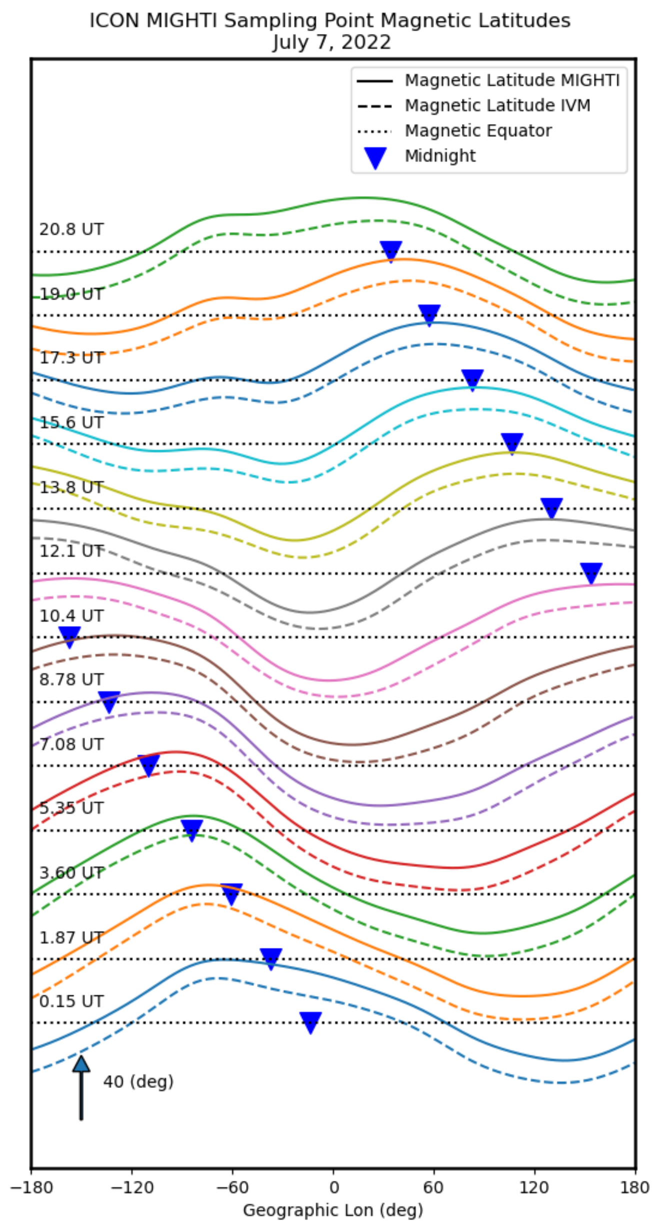

Figure 7. ICON MIGHTI side viewing limb sampling points and IVM situ measurement track. The MIGHTI has two viewing instruments A and B, they point towards rightside of the ICON satellite track with 45 degrees forward and 45 degrees backward respectively. The two orthogonal viewing direction samples then combined to form neutral wind vectors. The IVM makes in-situ measurements along the ICON satellite track. Because of that, the two measurements are off set from each other. The nighttime sector samplings are located between 30 to 40 magnetic latitudes.

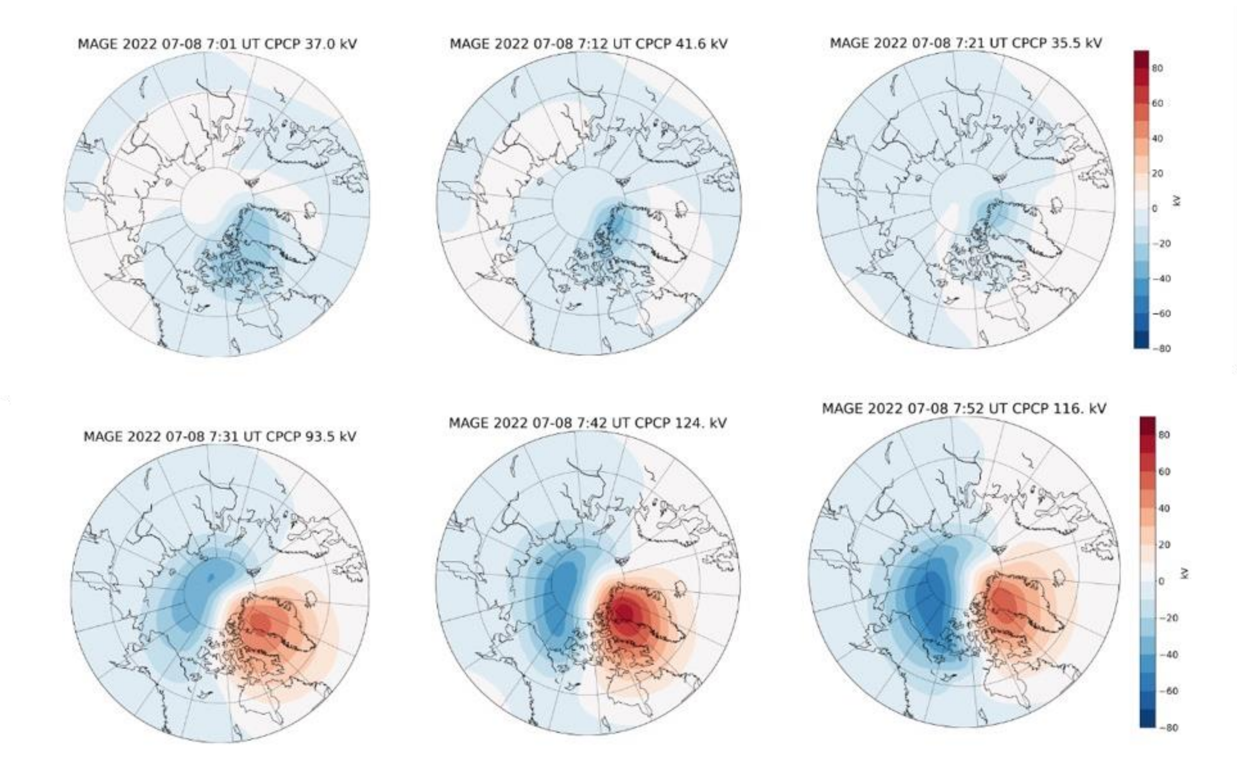

Figure 8. 8 July at 7-8 UT Polar cap potential map in the same format as Figure 3. The CPCP increased from 35.5 kV at 7:21 UT to 93.5 kV at 7:31 UT.

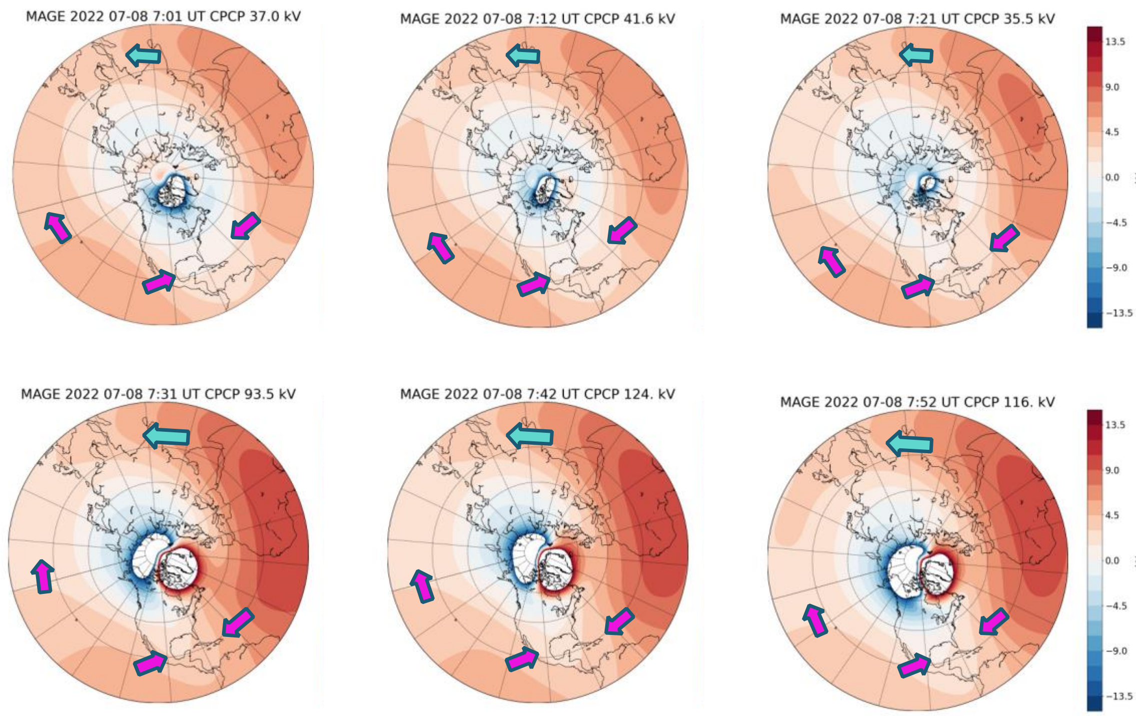

Figure 9. 8 July at 7-8 UT Global potential map in the same format as Figure 4. The potential pattern near the equator is more complex than in the case of 7 July at 12-13 UT, particularly on the nightside. There is a potential bulge that divides the nightside and causes a region near the midnight to have eastward electric field sandwiched between westward electric field (magenta color arrows). On the dayside the electric field is consistently eastward as indicated by the cyan color arrow.

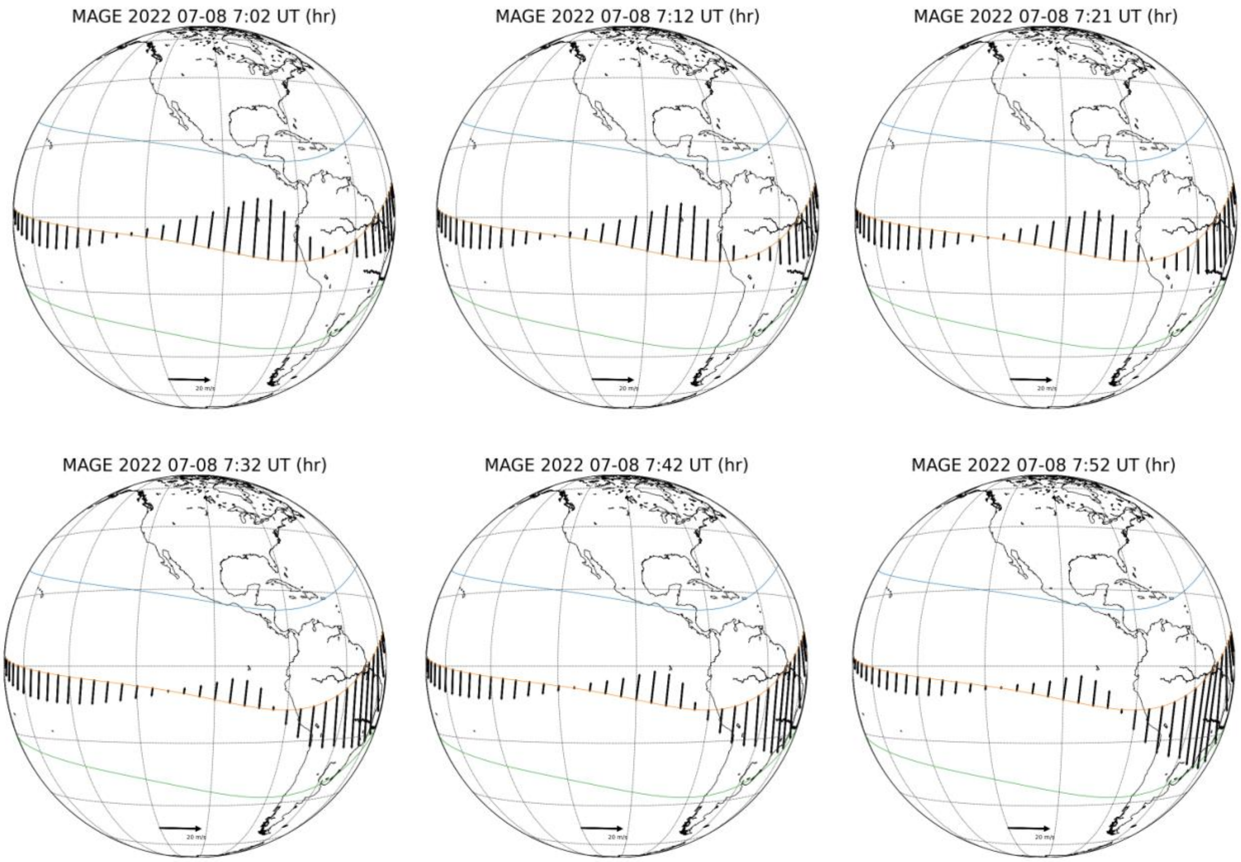

Figure 10. 8 July at 7-8 UT nightside equatorial vertical ion drift in the same format as Figure 5. Unlike the 7 July case, the nightside vertical ion drift is not uniformly downward. There is a region where the ion drifts are upward, consistent with the potential map in Figure 9 showing eastward electric field on the nightside.

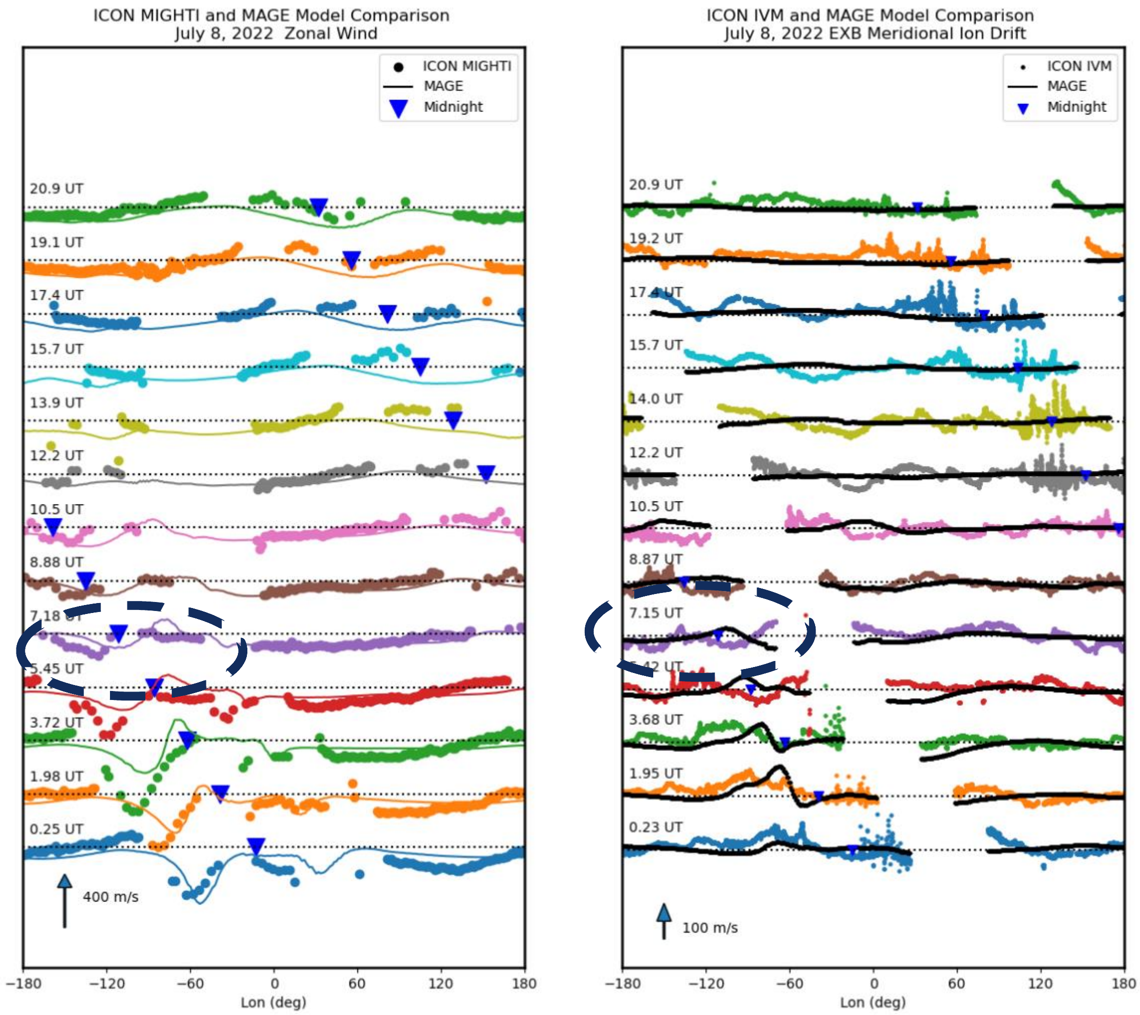

Figure 11. 8 July, MAGE simulation and ICON observation of zonal thermospheric winds and ion drifts in the same format as Figure 6. The orbit with the IMF Bz southward turning is highlighted by the dashed oval. Strong westward zonal wind on the nightside is prominent until 8 UT.

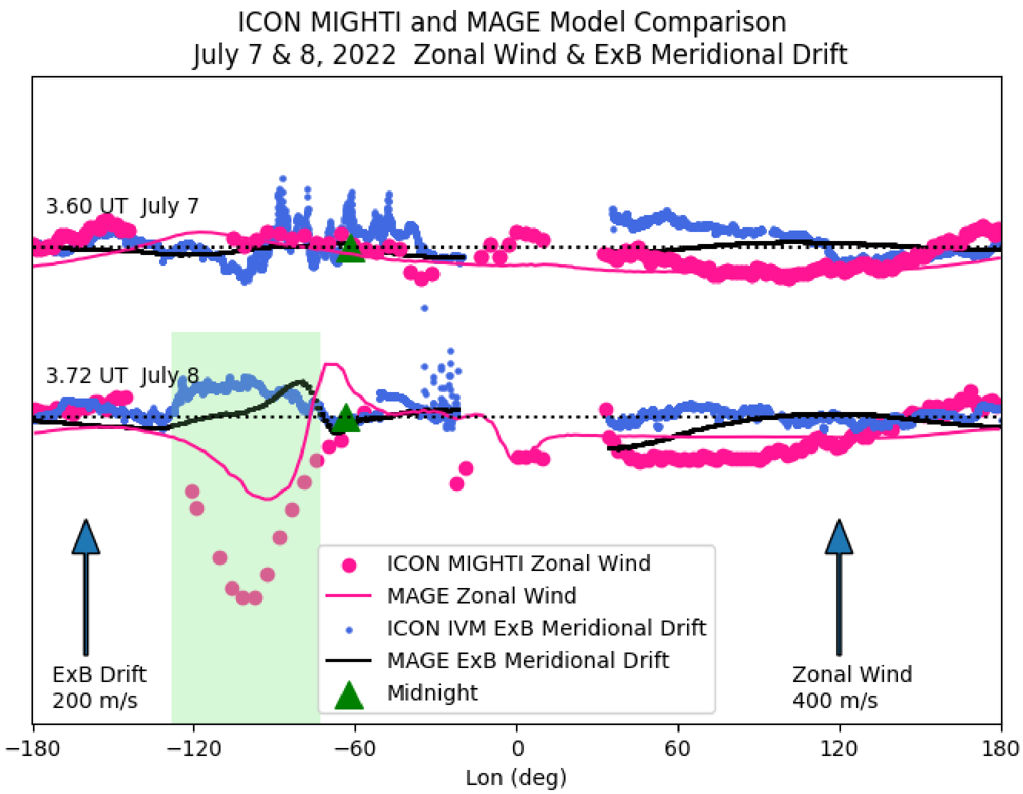

Figure 12. Comparison of the quiet (7 July, upper track) and disturbed (8 July, lower track) condition zonal wind and ExB ion drift observed by ICON MIGHTI (pink dots) and IVM (blue dots) and simulated by MAGE (pink line, and black line) during similar orbits. The highlighted area is a region of negative zonal wind with upward ion drift on 8 July.